

Development of a grain growth model for U_3Si_2 using experimental data, phase field simulation and molecular dynamics

Amani Cheniour^a, Michael R. Tonks^{a,*}, Bowen Gong^b, Tiankai Yao^c, Lingfeng He^c, Jason M. Harp^d, Benjamin Beeler^e, Yongfeng Zhang^f, Jie Lian^b

^a Department of Materials Science and Engineering, University of Florida, Gainesville, FL, 32611, USA

^b Department of Mechanical, Aerospace and Nuclear Engineering, Rensselaer Polytechnic Institute, Troy, NY, 12180, USA

^c Idaho National Laboratory, Idaho Falls, ID, 83402, USA

^d Oak Ridge National Laboratory, Oak Ridge, TN, 37830, USA

^e Department of Nuclear Engineering, North Carolina State University, Raleigh, NC, 27607, USA

^f Department of Engineering Physics, University of Wisconsin-Madison, Madison, WI, 53711, USA

HIGHLIGHTS

- The grain growth constant and activation energy were obtained from isothermal annealing experiments on U_3Si_2 lamellae.
- The grain growth geometric constant was calculated using several 3D phase field grain growth simulations.
- The grain boundary mobility was determined from experimental data, grain boundary energy, and phase field simulations.
- More grain growth occurs in U_3Si_2 than in UO_2 at 1200 K.
- Grain growth is more rapid in UO_2 than in U_3Si_2 at their respective centerline temperatures.

ARTICLE INFO

Article history:

Received 30 August 2019

Received in revised form

11 February 2020

Accepted 17 February 2020

Available online 22 February 2020

Keywords:

U_3Si_2

Grain growth

Isothermal annealing experiments

Phase field

Grain boundary mobility

ABSTRACT

The purpose of this work is to develop a model for normal grain growth in U_3Si_2 . The average grain boundary energy was determined from previously published molecular dynamics simulations. The grain growth kinetics were quantified at various temperatures by annealing nanocrystalline samples. The mobility was determined by comparing phase field grain growth simulations to the experimental data. From these various methods, we found that the average grain size D in U_3Si_2 can be estimated over time t using the equation $D^2 - D_0^2 = 2\alpha M \gamma t$, where D_0 is the initial average grain size, the geometry factor $\alpha = 0.96$, the average grain boundary mobility $M = 6.30 \times 10^{-18} e^{\frac{0.33\text{eV}}{k_b T}} \text{m}^4/(\text{Js})$ with the Boltzmann constant k_b and temperature T , and the average grain boundary energy has been found as a function of temperature, e.g. $\bar{\gamma} = 0.83 \text{ J/m}^2$ at 673 K.

© 2020 Elsevier B.V. All rights reserved.

1. Introduction

U_3Si_2 has emerged as an Accident Tolerant Fuel (ATF) that can potentially replace UO_2 in commercial Light Water Reactors (LWRs). Its primary advantages compared to UO_2 are a higher uranium density, which can increase power efficiency, and a better thermal conductivity, resulting in a safety enhancement in accident scenarios. Its primary disadvantages are a lower melting

temperature and more reactivity with water. In addition, much less is known about its material behavior at typical reactor conditions.

Polycrystalline materials such as U_3Si_2 are composed of a series of grains with different orientations. A grain boundary is a region where different crystal orientations meet, increasing the disorder of the material. The average size of the grains increases with time, to reduce the overall energy, in a phenomenon called grain growth. The increasing grain size impacts the fuel performance, changing the fracture behavior of the fuel [1–4] and decreasing fission gas release [5].

In normal grain growth, the applied pressure P_d on a grain boundary depends on its radius of curvature ρ and its energy γ , i.e.

* Corresponding author.

E-mail address: michael.tonks@ufl.edu (M.R. Tonks).

$$P_d = \frac{\gamma}{\rho} \quad (1)$$

The grain boundary moves at a velocity v that equals the product of the grain boundary mobility M with the difference between the driving pressure and the resistive pressure P_r (which difference is not allowed to go below zero)

$$v = \frac{d\rho}{dt} = M(P_d - P_r) \quad (2)$$

In addition to the grain boundary energy, other possible driving forces include stored elastic and plastic energy. Sources of resistive pressure include voids, pores, and precipitates. In this paper, we consider ideal grain growth with no other driving forces besides the grain boundary energy and no resistive pressure. The behavior of a grain boundary is highly dependent on its shape and on the misorientation between the two adjoining grains, such that the mobility and energy are highly anisotropic.

To describe the grain growth of a polycrystalline material, it is common to predict the change in the average grain size D with time. The average grain size can be related to the average radius of curvature $\bar{\rho}$, which drives the grain growth, as

$$D = \alpha^{\frac{1}{2}} \bar{\rho} \quad (3)$$

where α is a geometric constant that varies depending on the grain topology. If we take the derivative of this equation with respect to time and assume α is constant, we obtain

$$\frac{\partial D}{\partial t} = \alpha^{\frac{1}{2}} \frac{\partial \bar{\rho}}{\partial t} \quad (4)$$

By assuming that curvature is the only driving force and using Eq. (2) to eliminate $\bar{\rho}$, we obtain

$$\frac{\partial D}{\partial t} = \alpha \bar{M} \left(\frac{\bar{\gamma}}{D} - \alpha^{-\frac{1}{2}} P_r \right) \quad (5)$$

where $\bar{\gamma}$ and \bar{M} are the average grain boundary energy and mobility. Then, if we assume there is no resistive pressure and integrate with time, an expression can be developed to determine the average grain size as a function of time according to

$$D^2 - D_0^2 = 2\alpha \bar{M} \bar{\gamma} t \quad (6)$$

If the basic assumptions of this model, i.e. that the only significant driving force is curvature and there is no significant resistive pressure, are not true for a given material, it will not accurately describe the grain growth behavior for that material. In such cases, the exponent on D and D_0 is often fit to some other value, typically between 2 and 4. This has given rise to a semi-empirical model that is often fit to experimental data,

$$D^n - D_0^n = Kt \quad (7)$$

where K is a rate constant. For the special case where the assumptions made in Eq. (6) are valid ($n = 2$),

$$K = 2\alpha \bar{M} \bar{\gamma} \quad (8)$$

The goal of this work is to develop a model for U_3Si_2 grain growth driven by curvature and without significant resistive pressure, using Eq. (6). However, our model will be able to be naturally extended to consider resistive pressure due to porosity in future work. We obtain values for the average grain boundary energy $\bar{\gamma}$

Table 1

Table summarizing the results of the MD calculations of the U_3Si_2 average and standard deviation of the average grain boundary free energy at different temperatures from Ref. [6].

T (K)	$\bar{\gamma}$ (J/m ²)	σ_{γ} (J/m ²)
400	0.89	0.19
800	0.78	0.19
1200	0.62	0.20
1600	0.31	0.23

from existing molecular dynamics (MD) data [6], the kinetic parameter K from grain growth experiments on nanograined, fully dense samples, and the geometric factor α and the mobility M by comparing 3D mesoscale grain growth simulations with the experimental data. We begin by discussing the grain boundary energy in Section 2, and then the experiments in Section 3. The mesoscale grain growth simulations are summarized in Section 4. We then compare the grain growth in U_3Si_2 with that in UO_2 in Section 5.

2. Determination of the average grain boundary energy

The grain boundary energy of U_3Si_2 varies with misorientation and inclination, like with all materials. This anisotropy must be considered to accurately predict the behavior of individual grain boundaries. However, when modeling normal grain growth, this grain boundary anisotropy is averaged out and only the average energy need be considered. The grain boundary energy of U_3Si_2 has never been measured experimentally. Another effective means of determining the grain boundary energy of a material is using MD simulations, based on empirical potentials. This approach has been used for many materials, including Fe-Cr [7], Ni [8], and Al [9]. However, it can only be applied to materials with an existing empirical potential. An empirical potential has been recently developed for U_3Si_2 [10]. This potential has been applied to calculate the grain boundary energy [6] at different temperatures and misorientation angles. The average grain boundary energies at different temperatures from Ref. [6] are summarized in Table 1, as are their standard deviations. The average grain boundary energy (referred to as free energy in Ref. [6]) results from the sum of the enthalpy of formation per unit area $H(T)$ (referred to as grain boundary energy in Ref. [6]) and the entropy of formation per unit area $S(T)$ contributions according to

$$\bar{\gamma}(T) = H(T) - TS(T) \quad (9)$$

We have fit polynomials to the MD data for U_3Si_2 [6] to obtain expressions for the entropy and enthalpy contributions, giving

$$\begin{aligned} H(T) &= 1.21 \times 10^{-7} T^2 - 3.46 \times 10^{-5} T \\ &\quad + 0.85 \text{ J/m}^2 \\ S(T) &= 4.58 \times 10^{-7} T - 1.72 \times 10^{-4} \text{ J/m}^2 \text{K} \end{aligned} \quad (10)$$

where T is the temperature in K. The average grain boundary energy values from the MD simulations and the fit are shown in Fig. 1.

3. Determination of the kinetic parameter

The goal of the experimental work was to determine the kinetic parameter K for U_3Si_2 as a function of temperature. The kinetic parameter is known to follow an Arrhenius expression according to

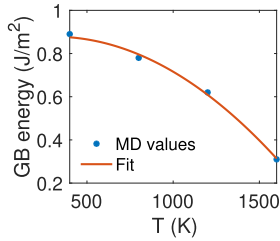


Fig. 1. The average grain boundary energy vs temperature calculated using MD simulations [6]. The fit expressed in Eqs (9) and (10) is also shown.

$$K = K_0 e^{-\frac{Q}{k_b T}}, \quad (11)$$

where Q is the activation energy, K_0 is the prefactor, T is the temperature and k_b is the Boltzmann constant. Q and K_0 were determined from measurements of the changing average grain size in U_3Si_2 at various temperatures.

A bulk U_3Si_2 sample was prepared by arc melting the powder mixture of uranium and silicon with near stoichiometric quantities, followed by inert atmosphere sintering at over 1673 K for several hours [11,12]. Lamellae were prepared using a focused ion beam (FIB) at the Center for Advanced Energy Studies (CAES) of Idaho National Laboratory with a FEI Quanta 3D FEG apparatus. A representative lamella prepared by FIB is shown in Fig. 2(A), the size of which is around $10 \times 10 \mu m$, with thickness being ~ 80 nm. The lamellae were then amorphized at room temperature with 1 MeV Kr^{2+} up to 0.4 dpa using the IVEM-Tandem facility at Argonne National Laboratory (ANL) to achieve a fully amorphous state, as evidenced by the amorphous halo in the SAED pattern shown in Fig. 2(B). The amorphized specimens were subsequently heated to allow for crystallization and the creation of high density ultrafine U_3Si_2 nanocrystals. A TEM image of amorphized U_3Si_2 is shown in Fig. 3(A) and the formation of the high-density nanocrystals of U_3Si_2 was clearly evidenced in Fig. 3(B). The diffraction pattern shown in Fig. 3(C) was indexed to the tetragonal U_3Si_2 , suggesting

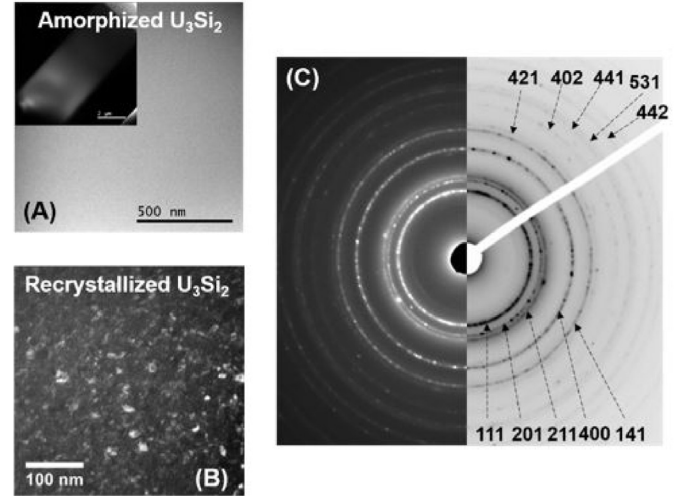


Fig. 3. Evidence of the crystallization of the U_3Si_2 samples: (A–B) Bright/dark field TEM images of the pre-amorphized and recrystallized U_3Si_2 , and (C) the indexing of the diffraction patterns to nano-sized U_3Si_2 .

the recrystallization and the formation of the nanocrystalline U_3Si_2 . These nanocrystalline samples had a high driving force for grain growth due to their small grain curvature, and since they were fully dense, there was no porosity to create resistive pressure. Thus, they were ideal for grain growth experiments.

The nanocrystalline lamellae were annealed at temperatures ranging from 523 K to 873 K to accelerate grain growth, during which bright field and dark field images and the corresponding selected area electron diffraction (SAED) patterns were recorded at various times during the annealing. A Hitachi H9000 intermediate voltage electron microscope (IVEM) with 300 KeV electron energies was utilized for the in-situ microstructure characterization. The temperature was carefully controlled through a double-tilt high temperature heating stage and the vacuum was controlled at $\sim 5 \times 10^{-8}$ torr to reduce the risk of oxidation and contamination. A

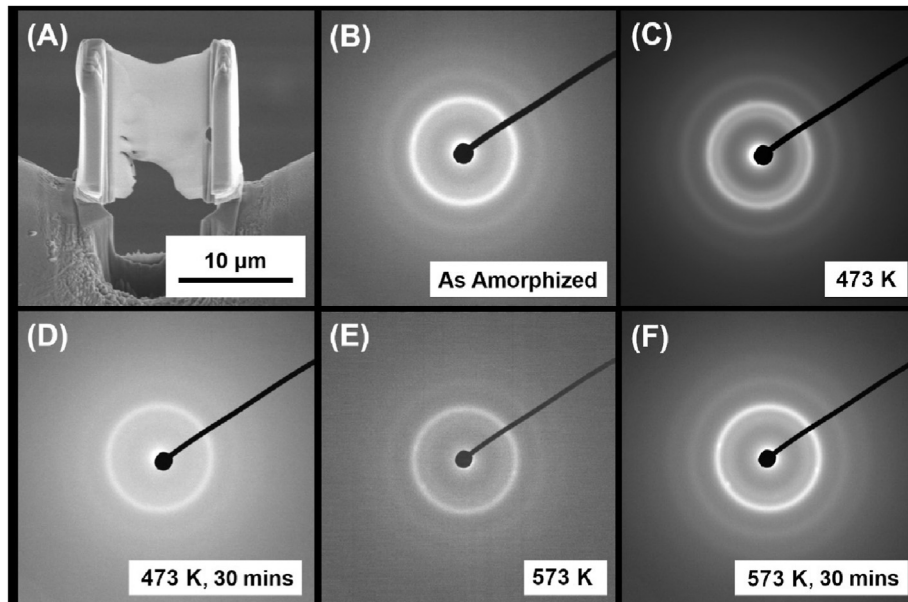


Fig. 2. Example of the crystallization of the amorphous samples: (A) FIB lamella of U_3Si_2 , (B–F) microstructure evolution of the pre-amorphized U_3Si_2 heat treated at different temperatures and durations. The recrystallization was initiated at 573 K for 30 min.

Gatan OneView digital camera was used to collect high resolution images. The average grain area at each time was manually calculated based on several randomly selected areas containing more than 30 grains with the image processing package ImageJ, and the grain size was determined by equating the area of a grain with the area of a circle. Statistical analysis was derived to obtain the average grain size and the associated standard deviation. As these are average grain sizes, they follow a normal distribution according to the mean value theorem. Note that the grain size values, and all other values throughout this work, are shown in the notation $A \pm B$, where A is the mean of the value and B is its standard deviation.

Isothermal annealing was carried out on one lamella at 673 K in order to fit values for the exponent n and kinetic coefficient K using Eq. (7). An amorphous lamella was annealed until it crystallized. Then, images were taken for determining the average grain size at eight times up to 86 min. Fig. 4 shows the images with the measured average grain sizes and their standard deviations from the isothermally annealed lamella. Once the average grain sizes were determined from the images, a polynomial curve was fit to the values versus time to determine the value for n . The fitted value was $n = 2$ within the experimental error, as demonstrated in Fig. 4(F), indicating that curvature was the only significant driving force for grain growth in the samples and that there was no significant pinning pressure. A linear fit of $D^2 - D_0^2$ vs time was used to determine the value for the kinetic coefficient K at 673 K, as shown in Fig. 4(G). However, this value does not include the uncertainty in the measured average grain sizes. To determine the distribution of K due to the uncertainty, 10,000 sets of grain size values at the eight times were sampled from normal distributions with the measured means and standard deviations for each annealing time. These values were used to calculate 10,000 different K values. A histogram approximation of the distribution of these 10,000 values indicated that K followed a normal distribution (Fig. 4(H)) with $K(673 \text{ K}) = 2.97 \pm 0.11 \times 10^{-20} \text{ m}^2/\text{s}$.

Ideally, the process carried out to determine a value for K at 673 K would be repeated at additional temperatures and then those values for K would be used to determine values for the activation energy Q and the prefactor K_0 such that K could be determined at any temperature using Eq. (11). However, due to limited time available on the specialized instruments used to collect the data,

this was not possible. Therefore, a different approach was used to determine values for Q and K_0 using only two additional lamellae. These two samples were annealed at a given temperature until they crystallized and an initial image was taken. Then they were heated and maintained at that temperature for a set amount of time to allow some grain growth, before taking another image. This was repeated twice for one lamella (using fairly short hold times) and thrice for the other (using longer hold times). The temperatures, times, average grain sizes, and grain size standard deviations for the two samples are shown in Fig. 5. The average grain sizes from these samples were used to determine a value for Q by comparing average grain size predictions using Eq. (6) with the measured values. For each initial grain size, final grain size, temperature and time, the final average grain size was predicted using a given value for Q . The value for K_0 was determined using Eq. (11) with the given Q value, $T = 673 \text{ K}$, and the $K(673 \text{ K})$ value determined from the isothermal annealing data. This calculation was repeated for 500 values of Q , ranging from 0.1 to 1.0, and the calculated average grain size was compared with the measured values. The error in each calculation was determined as the absolute value of the difference between the predicted and measured values. The root mean squared value of the five error values (two measured average grain sizes from the sample with short hold times and three from that with long hold times) was determined for each Q value. The minimum error was found to occur when $Q = 0.33 \text{ eV}$, with a corresponding

$$K_0 = K(673 \text{ K}) e^{\frac{Q}{k_b T}} = 8.77 \times 10^{-18} \text{ m}^2 / \text{s}, \quad (12)$$

as shown in Fig. 6(A). The measured grain sizes, as well as the predicted values using these values for Q and K_0 , are shown in Fig. 6(B). Thus, the rate constant $K = 8.77 \times 10^{-18} e^{-\frac{0.33}{k_b T}} \text{ m}^2/\text{s}$.

This approach requires only 13 total measurements of the average grain size (eight for the isothermal annealing and five more for the variable temperature samples), while determining K at various temperatures using isothermal annealing would have required around 40 measurements. However, it introduces more

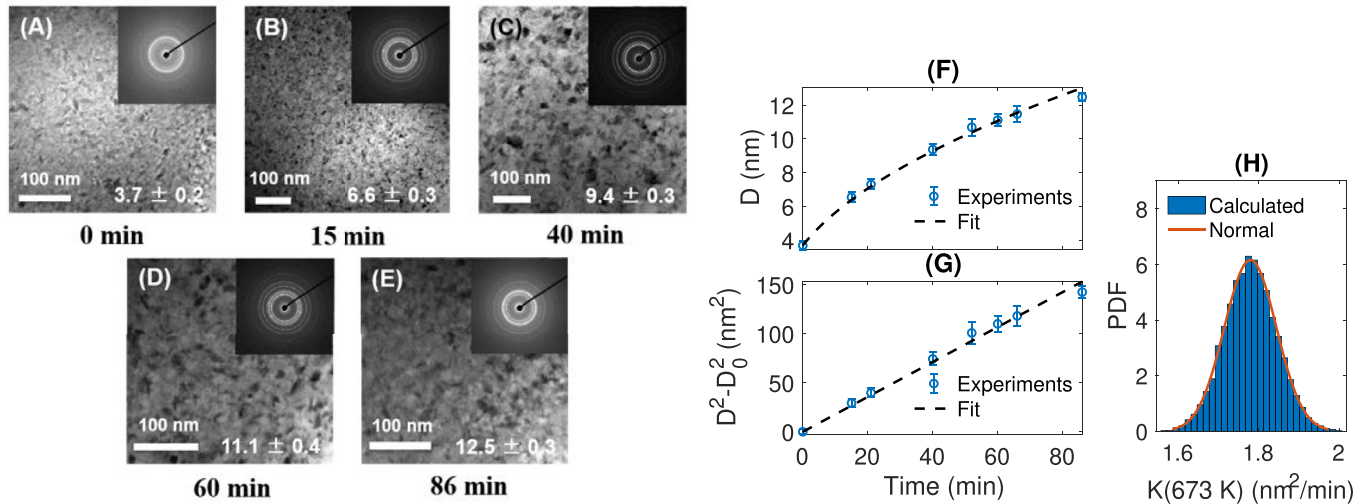


Fig. 4. Isothermal annealing-induced grain coarsening of the high density U_3Si_2 nanocrystals at 673 K for different durations. (A)–(E) show bright field images with the corresponding times and average grain sizes. Grain size increases monotonically with annealing time. A plot of the average grain size with time is shown in (F), fit with Eq. (7) using $n = 2$, indicating that curvature was the only significant driving force and that there was no significant pinning pressure. A linear fit of $D^2 - D_0^2$ with time t is shown in (G), where the slope of a linear fit to the data points is the value of K . A histogram approximation of the distribution of K is shown in (H) overlaid with a PDF of a normal distribution shown in orange. (For interpretation of the references to colour in this figure legend, the reader is referred to the Web version of this article.)

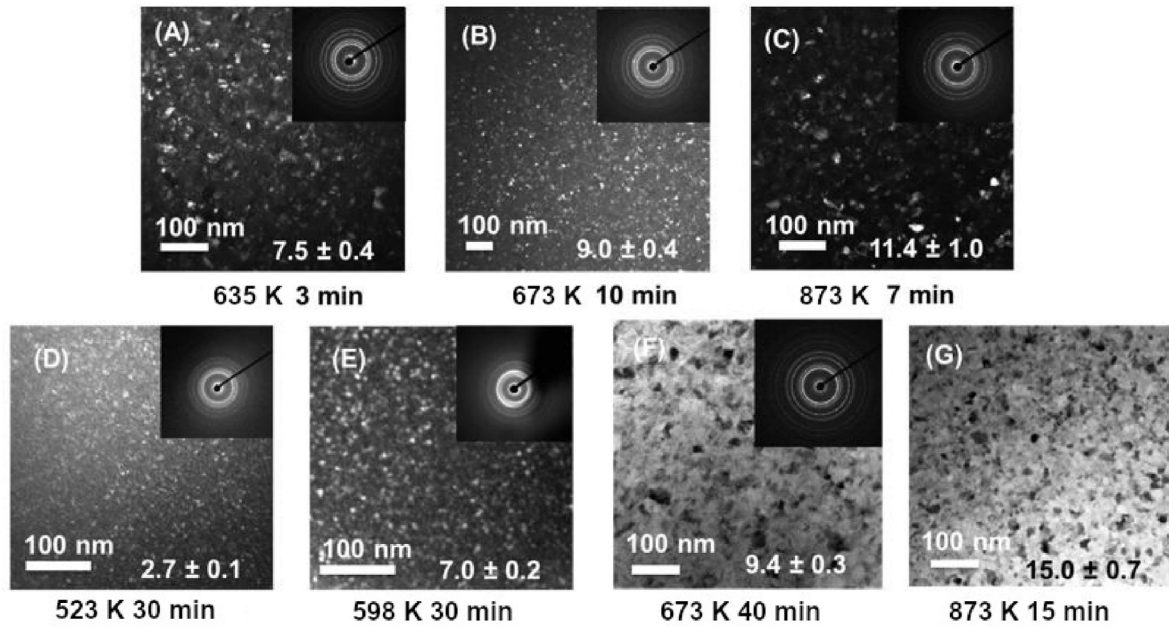


Fig. 5. Grain growth experiments carried out at increasing temperatures. (A) and (D) show the conditions and bright field images used to crystallize the samples with the initial grain size. (B) and (C) show the conditions, images, and average grain sizes in the lamella that used short annealing times. (E)–(G) show the conditions, images, and average grain sizes in the lamella that used long annealing times.

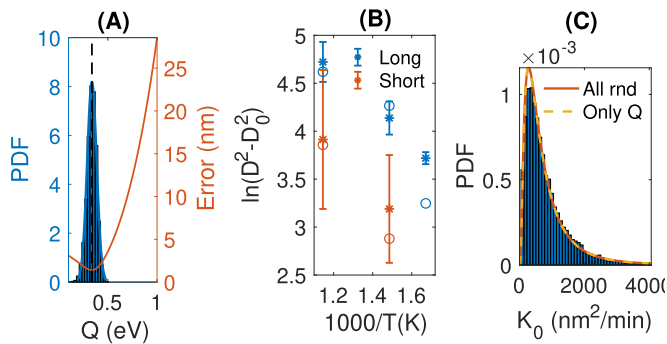


Fig. 6. Determination of Q by comparing predicted results to the measured values; (A) the RMS error value vs Q , where the dashed line shows the Q value that gives the minimum error ($Q = 0.33$ eV) and a histogram approximation of the distribution of Q (B) compares the predicted values using the optimal Q to experimental values, where the open circle are the predicted values; (C) histogram approximation of the distribution of K_0 (blue bars) and an overlaid lognormal distribution. The lognormal distribution if only Q is treated as random is also shown, directly overlapping the distribution with both dependent variables random, indicating that uncertainty in Q dominates the distribution. (For interpretation of the references to colour in this figure legend, the reader is referred to the Web version of this article.)

error in the final value. Thus, it is critical to quantify the uncertainty in the values for K_0 and Q that we have determined. We repeated the approach for determining the value for Q illustrated in Fig. 6(A) 10,000 times with values for the five measured grain sizes randomly sampled from normal distributions with means and standard deviations corresponding to the measured values. From this approach, Q was found to approximately follow a normal distribution with a standard deviation of 0.05 eV, as shown in Fig. 6(A). Since the value for K_0 was determined using Eq. (12), its value depends on the values for both Q and $K(673\text{ K})$ and will thus have uncertainty due to the uncertainty in both those values; K_0 follows a lognormal distribution, as shown in Fig. 6(C). However, it is not an independent random variable and its random value must be determined from Eq. (12) using random values for Q and $K(400^\circ\text{C})$.

If we only treat Q as a random variable and assume the $K(673\text{ K})$ is not random, the distribution is unchanged (see Fig. 6(C)) indicating that the uncertainty in Q dominates the distribution of K_0 .

4. Determination of the grain boundary mobility

The grain boundary mobility can be obtained from the kinetic parameter K using Eq. (8). To determine the mobility requires a value for the average grain boundary energy $\bar{\gamma}$, which we have obtained from published MD data as discussed in Section 2, and a value for the shape factor α . In this section, we first determine the value of α using phase field grain growth simulations and then calculate the grain boundary mobility.

The kinetic parameter K was determined from average grain sizes from 2D images of the surface of the 3D lamellae. The shape factor α relates this average grain size D from the sample surface to the 3D average grain boundary curvature $\bar{\rho}$ that drives the actual grain growth behavior according to Eq. (3). The shape factor is often assumed to be one [13], to simplify Eq. (8), but we will investigate its value using 3D simulations. In 2D grain growth simulations the value has been found to be 0.5 [14], but the value in 3D will likely vary from this value. To calculate α in this work, we modeled normal grain growth in 3D using a phase field method, as explained below. An example phase field domain is shown in Fig. 7(A).

4.1. The phase field model

Grain growth has been modeled using the phase field method for many years [15–19]. This method has also been successfully applied to model many other microstructure evolution phenomena, including solidification, Ostwald ripening, and recrystallization [20–23]. The phase field grain growth model uses phase field variables η_i to describe the grains. Each of these variables is equal to one inside corresponding grains and to zero in all other grains; they vary smoothly across the interface between grains, as shown in Fig. 7(B). The evolution of these variables depends on the change in the Gibbs free energy, which drives the system towards equilibrium

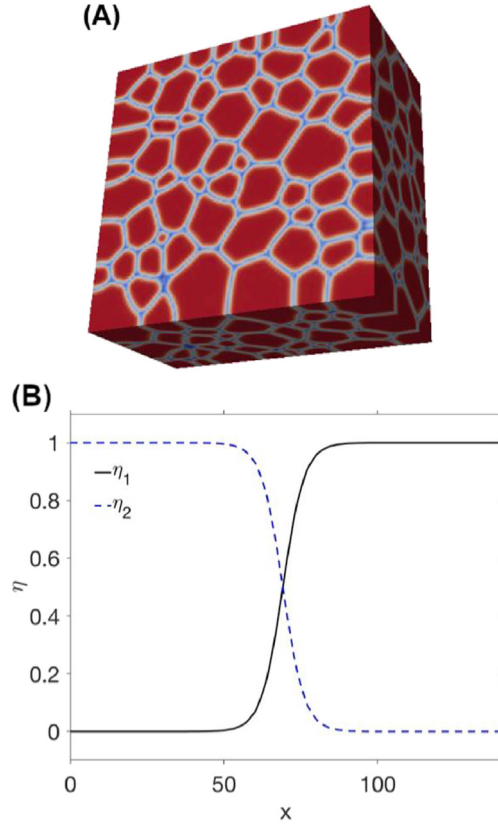


Fig. 7. Example of the 3D phase field grain growth simulations used to determine α : (A) shows an example of the 3D phase field domain with grains shown in red and grain boundaries in blue; (B) shows two phase field order parameters representing adjacent grains across a grain boundary. (For interpretation of the references to colour in this figure legend, the reader is referred to the Web version of this article.)

when reduced. This relationship corresponds to the Allen-Cahn equation:

$$\frac{\partial \eta_j}{\partial t} = -L_j \frac{\delta F}{\delta \eta_j}, \quad (13)$$

where L_j is the phase mobility and F the total free energy defined as [24].

$$F = \int_V \left[m f_{loc}(\eta_1, \dots, \eta_p) + \frac{k}{2} \sum_{i=1}^p (\nabla \eta_i)^2 \right] dV, \quad (14)$$

where f_{loc} is the local free energy density function, m is a scalar multiplier, and the final term is the interfacial free energy that penalizes non-zero gradients of the variables across the grain boundary [24].

To accurately capture grain growth, it is important to choose the local free energy expression correctly. The free energy developed in Ref. [24] has the advantage of having been proven to quantitatively describe the change in grain size. This expression is

$$f_{loc} = \sum_i^N \left(\frac{\eta_i^4}{4} - \frac{\eta_i^2}{2} \right) + \frac{3}{2} \sum_{i=1}^N \sum_{j>i}^N \eta_i^2 \eta_j^2 + \frac{1}{4}, \quad (15)$$

where the model parameters L , m , and κ are expressed as functions of the grain boundary energy γ , mobility M , and width ω [24]. In this work we assume that the grain boundary energy and mobility

are isotropic so we use a single average grain boundary energy $\bar{\gamma}$ and mobility \bar{M} for all grain boundaries. The grain boundary width ω is the width of the diffuse interface that represents the grain boundary and it must be adequately resolved in order to accurately predict the grain boundary migration. Therefore, it is typically selected as a model parameter that is orders of magnitude larger than the actual grain boundary width. It must be chosen to be much smaller than the grain size to avoid incorrect results but larger than the real grain boundary width to improve computational efficiency.

This grain growth model is implemented using the finite-element method (FEM) and implicit time integration with MARMOT [25], a mesoscale fuel performance code designed to simulate the microstructure evolution and change in material properties of nuclear fuels using the phase field method. MARMOT derives from the Multiphysics Object-Oriented Simulation Environment (MOOSE) framework [26]. All grain growth simulations in this work were performed using MARMOT to solve Eq. (13). The FEM shape functions for the order parameters were first-order Lagrange functions. The domain size was chosen to be $150 \times 150 \times 80$ nm, as shown in Fig. 7(A), since the thickness of the experimental lamellae was 80 nm. The initial number of grains was between 500 and 600 to obtain at least 100 grains on the top and bottom $150 \text{ nm} \times 150 \text{ nm}$ surfaces and the grains were represented using 28 variables. The latter is smaller than the number of grains because we used the Grain Tracker algorithm [27] available in MOOSE, which makes it possible to use variables to represent multiple grains and still avoid grain coalescence. This drastically reduces the computational cost. Multiple initial grain structures were created using different random seeds with a Voronoi tessellation. All boundaries were given a zero-flux condition. The grain boundary width ω was chosen to be 3 nm. Mesh and time step adaptivity were used to decrease the computational cost, with the element size ranging from 4 nm^3 to 2083 nm^3 and the time step size ranging from 100 s to 1600 s.

4.2. Simulation results

The objective of these simulations was to determine a value of α that relates the average grain size D determined from a 2D surface to the average radius of curvature $\bar{\rho}$. This was achieved by running simulations with specific values of the grain boundary mobility M_{sim} and energy γ_{sim} . The simulations predicted the change in the average grain size with time, and the grain size values were used to obtain rate constant K_{sim} values. The value of α was obtained by solving Eq. (8) for α to get

$$\alpha = \frac{K_{sim}}{2M_{sim}\gamma_{sim}}. \quad (16)$$

For these calculations, we used $\gamma_{sim} = 0.834 \text{ J/m}^2$ (calculated using Eq. (10) at 673 K) and $M_{sim} = 1.78 \times 10^{-20} \text{ m}^4/(\text{J s})$. The phase field simulations and resultant calculation of α were repeated for different initial grain configurations to determine an estimate of the error in the α value.

For each initial grain configuration, the average grain size was calculated from the average grain area on a surface, similar to what was done in the experiments. First, the average grain area was determined by dividing the area of the top boundary of the simulation domain by the current number of grains on that boundary. The average grain size was then calculated by assuming circular grains. This process was repeated at various times, and the values were then fit using Eq. (11) to determine a value for K from the simulations (illustrated in Fig. 8). The value for α was calculated using Eq. (16).

In addition to the values for K and α calculated from the grain

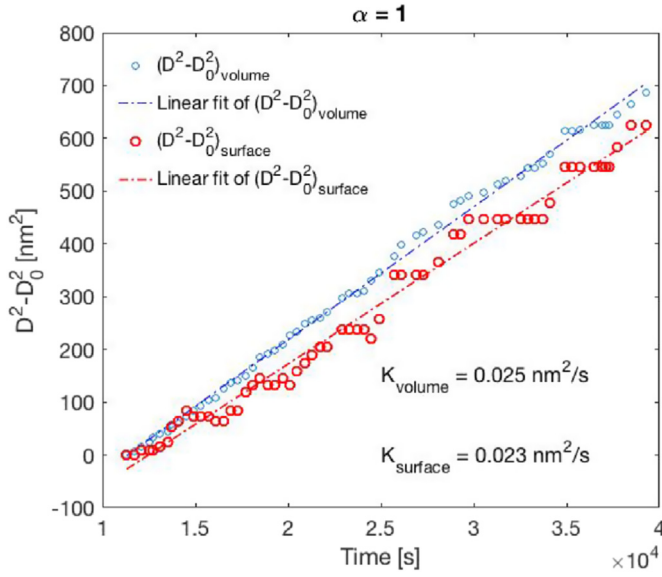


Fig. 8. Demonstration of the process used to determine the values for K from the phase field simulation results assuming $\alpha = 1$.

size estimated from a surface, we also determined their values from grain sizes estimated from the entire volume of the material. The purpose of this was to determine if there was any error introduced by our use of surface data from the lamella to evaluate the value for K .

We carried out five simulations, each with a different grain structure. For each simulation, the change in D^2 was not linear with time at the beginning of the simulation, due to the initial grain structure from the Voronoi tessellation. Therefore, data was not collected until after the change in D^2 became linear with time. Within the linear region, a line was fit to the grain size values from the simulation results over time as demonstrated in Fig. 8. This process was repeated for all the simulation results. Note that volume grain size data has less scatter than the surface data because all of the grains were averaged for the volume calculation while only the grains on the surface were averaged for the surface calculation. However, we still use the surface data as our primary means of estimating α , since it most closely relates to the approach used in the experiments.

The mean values of K and α from the surface and volume grain sizes (K_{surface} , K_{volume} , α_{surface} , and α_{volume}) and their standard deviations are shown in Table 2. Note that K_{volume} and α_{volume} have smaller standard deviations than their corresponding surface values because of the reduced scatter in the grain size data, as mentioned previously. The average value of α using the surface grain sizes is 0.96, with a standard deviation of 0.18. The volume value only varied from the surface value by a small amount ($\alpha_{\text{volume}} = 1.04$), indicating that the results are not significantly impacted by calculating the grain sizes from surface data.

With the value for α , we have everything needed to calculate the average grain boundary mobility using Eq. (8). As with K , the average mobility \bar{M} can be expressed as an Arrhenius expression according to Eq. (17):

$$\bar{M} = M_0 e^{-\frac{Q}{k_b T}}, \quad (17)$$

where M_0 is the pre-exponential factor and $Q = 0.33$ eV is the same activation energy as from K (with the same distribution). Solving Eq. (8) for M and substituting Eqs (11) and (17), we obtain

Table 2

Table summarizing the results of the phase field simulations of grain growth in U_3Si_2 : average grain growth constants K_{surface} and K_{volume} and average values for α_{surface} and α_{volume} with their respective standard deviations.

Quantity	Average	Standard deviation
K_{surface} (nm^2/s)	0.028	0.0053
K_{volume} (nm^2/s)	0.031	0.0039
α_{surface}	0.96	0.18
α_{volume}	1.04	0.15

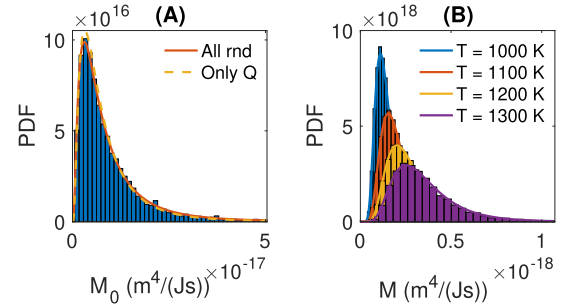


Fig. 9. The histogram approximations of M_0 and M ; (A) shows the distribution of the calculated values for M_0 , where the blue bars are the histogram and the blue line is the fitted lognormal distribution; (B) shows the distribution of M at different values of T , where the bars are the histogram and the lines are the fitted lognormal distribution. (For interpretation of the references to colour in this figure legend, the reader is referred to the Web version of this article.)

$$M_0 e^{-\frac{Q}{k_b T}} = \frac{K_0}{2\alpha\bar{\gamma}} e^{-\frac{Q}{k_b T}}. \quad (18)$$

Then, canceling the exponential term and using Eq. (12) and the values for $\bar{\gamma}$, and α gives

$$M_0 = \frac{K(673 \text{ K})}{2\alpha\bar{\gamma}(673 \text{ K})} e^{\frac{Q}{k_b 673.15}} = 6.30 \times 10^{-18} \text{ m}^4/(\text{Js}). \quad (19)$$

This value is uncertain due to the uncertainty in the values of $K(673 \text{ K})$, α , $\bar{\gamma}$ and Q . We generated 10,000 random values from each random variable and the resultant value followed a lognormal distribution, as shown in Fig. 9. However, just like K_0 , M_0 is not an independent random variable; its random value must be determined from Eq. (19) using random values for $K(400^\circ\text{C})$, α , $\bar{\gamma}$ and Q . Also, like K_0 , when only Q is considered random the distribution is not significantly changed, indicating that Q is the dominate source of uncertainty. The mobility at a given temperature is also a random dependent variable calculated according to Eq. (17), as shown in Fig. 9(B), or $\bar{M} = 6.30 \times 10^{-18} e^{-\frac{0.33 \text{ eV}}{k_b T}} \text{ m}^4/(\text{Js})$.

5. Comparison with UO_2

Using the value for $\bar{\gamma}$ from Section 2 and the expression for α and \bar{M} from the previous section, we can use Eq. (6) to predict the average grain size with time in fully dense U_3Si_2 for which curvature is the only significant driving force. In sintered U_3Si_2 , which will not be fully dense, there would be some resistive pressure due to porosity that would have to be considered.

In order to provide some context for the grain growth behavior of U_3Si_2 , in this section we compare it with the grain growth behavior in UO_2 , as measured by Ainscough et al. [28]. Ainscough et al. did not determine the grain boundary mobility, but rather the

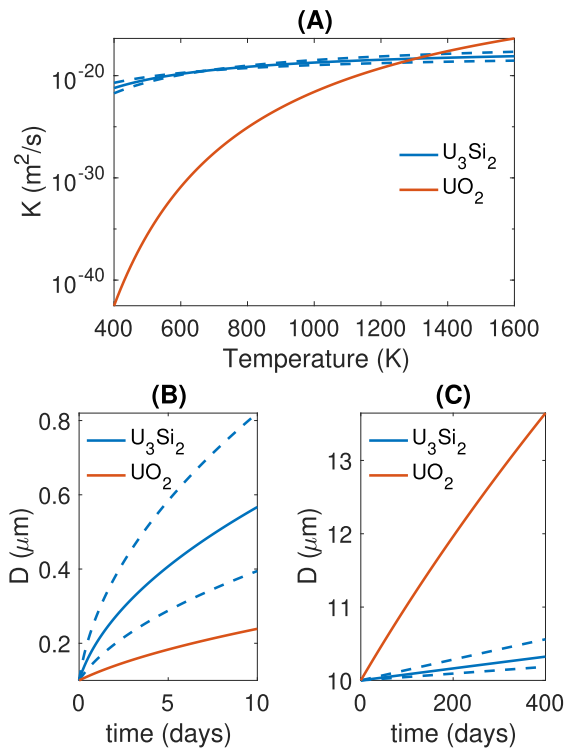


Fig. 10. Comparison between the grain growth behavior of UO_2 and U_3Si_2 , where (A) shows a plot of the kinetic parameter K , (B) shows the evolution of grain size with time at 1200 K, and (C) shows the evolution of the grain size with time for representative centerline temperatures of the two materials at LWR conditions: 1000 K for U_3Si_2 and 1400 K for UO_2 . Dashed lines are used to represent values for U_3Si_2 using $Q \pm 2\sigma_Q$, to show the impact of the uncertainty in Q on the predicted values.

kinetic parameter K , so we will begin by comparing the kinetic parameters. In addition, they determined their K value using grain sizes obtained using linear intercept values without conversion. To convert their K values to those obtained from standard grain size values, we multiply their value by 1.571 as dictated by the ASTM standard [29]. The kinetic parameters for U_3Si_2 and UO_2 are compared in Fig. 10(a). We calculate K in U_3Si_2 using the mean values of K_0 and Q , but we also show K when the value for Q is increased and decreased by two standard deviations σ_Q (we only consider the impact of variation in Q since its uncertainty was shown to dominate the distribution of K_0). In UO_2 , the activation energy $Q = 2.77$ eV, while in U_3Si_2 $Q = 0.33$ eV. For this reason, the value for K changes much more dramatically with temperature in UO_2 than in U_3Si_2 such that K is larger in U_3Si_2 below 1300 K, but it is larger in UO_2 above 1300 K. The impact of the uncertainty in the K for U_3Si_2 is evident, but small compared to the large changes with temperature in the UO_2 value.

Next we simulate the grain growth in both materials at 1200 K. We predict the growth using Eq. (7) with $n = 2$. We assume an initial grain size in both materials of 0.1 μm . The change in the average grain size of each material with time is shown in Fig. 10(b). The impact of uncertainty in the U_3Si_2 grain size is also shown. After 10 days at the elevated temperature, the U_3Si_2 will have reached an average grain size of 0.57 μm , while the UO_2 will have only reached a grain size of 0.24 μm . If we consider the uncertainty in Q with the U_3Si_2 model (using values $Q \pm 2\sigma_Q$), there is 95% confidence that the final average grain size will range between 0.39 μm and 0.82 μm . In order to reduce this uncertainty, additional experiments would need to be carried out to reduce the uncertainty in the value for Q .

Since U_3Si_2 has a higher thermal conductivity than UO_2 at

elevated temperatures, U_3Si_2 will operate at lower temperatures than UO_2 with the same reactor conditions. Metzger et al. [30], used BISON [31,32] simulations to determine the temperatures in both fuels at different positions within the fuel pellets. While the UO_2 centerline temperature was around 1400 K at the beginning of the fuel lifetime, the same conditions applied to U_3Si_2 resulted in a centerline temperature of approximately 1000 K. It is therefore intriguing to investigate grain growth at the fuel centerline temperature for each fuel type. Therefore, we model the grain growth of the two fuels at their relative centerline temperatures for 400 days, with an initial grain size of 10 μm , a common initial average grain size in UO_2 fuel pellets. Fig. 10(c) reveals that after 400 days, the average grain size in UO_2 has reached 13.65 μm while it has only reached 10.32 μm in U_3Si_2 (considering uncertainty, it will range between 10.19 μm and 10.56 μm with 95% confidence). This is because K in UO_2 at 1400 K is larger than K in U_3Si_2 at 1000 K.

6. Conclusion

In this work, we have developed a model for normal grain growth in U_3Si_2 , a LWR fuel candidate. The main properties required for the model are the average grain boundary energy $\bar{\gamma}$ and mobility \bar{M} and the shape factor α . An expression for the average grain boundary energy was obtained by creating a fit to temperature of values calculated using MD simulations. Isothermal annealing of U_3Si_2 lamellae was performed at 673 K to determine the rate constant K at that temperature. To find the value of the activation energy Q , two U_3Si_2 lamellae were held for specific times at increasing temperatures and the grain size was measured. Q was estimated to be 0.33 eV in U_3Si_2 by comparing model predictions with the measured values. This approach reduced the number of required samples, but increased uncertainty in the values; thus, uncertainties in both K_0 and Q were also estimated. The shape factor α was determined using 3D phase field grain growth simulations, giving $\alpha = 0.96$. By combining $\bar{\gamma}$, K , and α , we found the average grain boundary mobility $\bar{M} = 6.30 \times 10^{-18} e^{\frac{0.33 \text{ eV}}{k_B T}} \text{ m}^4/(\text{Js})$.

Since U_3Si_2 is being considered as an alternative to UO_2 , it is important to compare the grain growth behavior of both fuels. The rate constant K in UO_2 (taken from Ainscough et al. [28]) is smaller than K in U_3Si_2 at low temperatures but it is larger at temperatures higher than 1300 K. Thus, at 1200 K, grain growth occurs faster in U_3Si_2 . However, at typical reactor fuel centerline temperatures for the two fuels, U_3Si_2 will experience significantly less grain growth than UO_2 . The uncertainty in the grain growth predictions for U_3Si_2 is significant due to the uncertainty in the activation energy Q . This uncertainty should be reduced in the future using new grain growth data.

Finally, the authors emphasize the importance of addressing the impact of resistive pressure in future work. In reality, depending on the experimental technique used to prepare the sample, secondary phases and impurities may be present at grain boundaries and within the grains [33,34] and will resist grain boundary migration. Additionally, during reactor operation fission products are likely to segregate at grain boundaries. This can result in the formation of other phases [33] and fission gas bubbles that will also resist the migration.

Data availability

Data will be provided on request.

CRediT authorship contribution statement

Amani Cheniour: Software, Formal analysis, Validation, Writing - original draft. **Michael R. Tonks:** Conceptualization, Funding

acquisition, Project administration, Writing - review & editing. **Bowen Gong:** Investigation, Formal analysis, Writing - review & editing. **Tiankai Yao:** Investigation, Formal analysis, Writing - review & editing. **Lingfeng He:** Investigation, Writing - review & editing. **Jason M. Harp:** Resources, Writing - review & editing. **Benjamin Beeler:** Investigation, Formal analysis, Writing - review & editing. **Yongfeng Zhang:** Conceptualization, Project administration, Writing - review & editing. **Jie Lian:** Conceptualization, Project administration, Writing - review & editing.

Acknowledgments

This work was supported by the U.S. Department of Energy, Office of Nuclear Energy under a Nuclear Energy University Program (award number: 16–10667) and a NSUF RTE award (award number: 19–1691) under DOE Idaho Operations Office Contract DE-AC07-051D14517 as part of a Nuclear Science User Facilities Experiments.

Appendix A. Supplementary data

Supplementary data to this article can be found online at <https://doi.org/10.1016/j.jnucmat.2020.152069>.

References

- [1] R.W. Davidge, A.G. Evans, *J. Nucl. Mater.* 33 (1969) 249–260.
- [2] M. Oguma, *J. Nucl. Sci. Technol.* 19 (1982) 1005–1014.
- [3] K. Kapoor, A. Ahmad, A. Lakshminarayana, G.V. Hemanth Rao, *J. Nucl. Mater.* 366 (2007) 87–98.
- [4] Y. Zhang, P. Millett, M. Tonks, X.-M. Bai, S. Biner, in: *Int. Nucl. Fuel Cycle Conf. Glob. 2013 Nucl. Energy a Crossroads 2*, 2013.
- [5] K. Forsberg, A.R. Massih, in: *Proc. 16th Int. Conf. Struct. Mech. React. Technol.*, 2001.
- [6] B. Beeler, M. Baskes, D. Andersson, M.W. Cooper, Y. Zhang, *J. Nucl. Mater.* 514 (2019) 290–298.
- [7] Y. Shibuta, S. Takamoto, T. Suzuki, *Comput. Mater. Sci.* 44 (2009) 1025–1029.
- [8] S.M. Foiles, *Scripta Mater.* 62 (2010) 231–234.
- [9] K. Barmak, J. Kim, C.-S. Kim, W. Archibald, G. Rohrer, A. Rollett, D. Kinderlehrer, S. Ta'Asan, H. Zhang, D. Srolovitz, *Scripta Mater.* 54 (2006) 1059–1063.
- [10] B. Beeler, M. Baskes, D. Andersson, M.W. Cooper, Y. Zhang, *J. Nucl. Mater.* 495 (2017) 267–276.
- [11] T. Yao, B. Gong, L. He, J. Harp, M. Tonks, J. Lian, *J. Nucl. Mater.* 498 (2018) 169–175.
- [12] J.M. Harp, P.A. Lessing, R.E. Hoggan, *J. Nucl. Mater.* 466 (2015) 728–738.
- [13] J. Powers, A. Glaeser, *Interface Sci.* 6 (1998) 23–39.
- [14] M.R. Tonks, Y. Zhang, X. Bai, P.C. Millett, *Materials Research Letters* 2 (2014) 23–28.
- [15] D. Fan, L.-Q. Chen, *Acta Mater.* 45 (1997) 611–622.
- [16] N. Moelans, B. Blanpain, P. Wollants, *Acta Mater.* 53 (2005) 1771–1781.
- [17] Y. Suwa, Y. Saito, *Mater. Trans.* 44 (2005) 2245–2251.
- [18] N. Moelans, F. Wendler, B. Nestler, *Comput. Mater. Sci.* 46 (2009) 479–490.
- [19] H.G. Kim, J.H. Yang, W.J. Kim, Y.H. Koo, *Nucl. Eng. Technol.* 48 (2016) 1–15.
- [20] D.M. Anderson, G.B. McFadden, A.A. Wheeler, *Phys. Nonlinear Phenom.* 135 (2000) 175–194.
- [21] F. Yu, Y. Wei, Y. Ji, L.Q. Chen, *J. Mater. Process. Technol.* 255 (2018) 285–293.
- [22] L.-Q. Chen, S.P. Chen, P.W. Voorhees, D. Fan, *Comput. Mater. Sci.* 9 (1998) 329–336.
- [23] T. Takaki, Y. Hisakuni, T. Hirouchi, A. Yamanaka, Y. Tomita, *Comput. Mater. Sci.* 45 (2009) 881–888.
- [24] N. Moelans, B. Blanpain, P. Wollants, *Calphad Comput. Coupling Phase Diagrams Thermochem.* 32 (2008) 268–294.
- [25] M.R. Tonks, D. Gaston, P.C. Millett, D. Andrs, P. Talbot, *Comput. Mater. Sci.* 51 (2012) 20–29.
- [26] D. Gaston, C. Newman, G. Hansen, D. Lebrun-Grandié, *Nucl. Eng. Des.* 239 (2009) 1768–1778.
- [27] C.J. Permann, M.R. Tonks, B. Fromm, D.R. Gaston, *Comput. Mater. Sci.* 115 (2016) 18–25.
- [28] J.B. Ainscough, J. O. Ware 49 (1973) 117–128.
- [29] *Standard Test Methods for Determining Average Grain Size*, ASTM International, West Conshohocken, PA, 2013. Standard ASTM E112–13.
- [30] K.E. Metzger, T.W. Knight, R.L. Williamson, *Proc. ICAPP 2014* (2014) 2279–2286.
- [31] R.L. Williamson, J.D. Hales, S.R. Novascone, M.R. Tonks, D.R. Gaston, C.J. Permann, D. Andrs, R.C. Martineau, *J. Nucl. Mater.* 423 (2012) 149–163.
- [32] J.D. Hales, R.L. Williamson, S.R. Novascone, D.M. Perez, B.W. Spencer, G. Pastore, *J. Nucl. Mater.* 443 (2013) 531–543.
- [33] D.A. Lopes, A. Benarosch, S. Middleburgh, K.D. Johnson, *J. Nucl. Mater.* 496 (2017) 234–241.
- [34] J. White, A. Nelson, J. Dunwoody, D. Byler, D. Safarik, K. McClellan, *J. Nucl. Mater.* 464 (2015) 275–280.